ISSN 0915-633X

NATIONAL INSTITUTE FOR FUSION SCIENCE

Generation Mechanism of a Dipole Field by a Magnetohydrodynamic Dynamo

A. Kageyama and T. Sato

(Received - Sep. 20, 1996)

NIFS-458 Oct. 1996

RESEARCH REPORT
NIFS Series

NAGOYA, JAPAN

Generation Mechanism of a Dipole Field by a Magnetohydrodynamic Dynamo

Akira Kageyama and Tetsuya Sato

Theory and Computer Simulation Center, National Institute for Fusion Science, Nagoya 464-01, Japan

Computer simulation of a magnetohydrodynamic dynamo in a rotating spherical shell is performed. Strong magnetic field is generated by a thermal convection motion of an electrically conducting fluid. The generated magnetic field has a well-organized structure. The field is expanded by the spherical harmonics Y_ℓ^m. The leading moment is the dipole ($\ell = 1, m = 0$) which is 1.3 times larger than the second moment, octapole ($\ell = 3, m = 0$). These two moments occupy more than half of the total power of the magnetic field. Structure and the generation mechanism of the magnetic field are examined in detail. It is found that the well-known α-ω dynamo scenario gives a good explanation of the whole dynamo cycle. This simulation gives the first demonstration that a self-consistently solved magnetohydrodynamic convection naturally produces the α-ω dynamo and the dipole field is spontaneously generated.

keywords MHD dynamo, solar dynamo, geodynamo

I. INTRODUCTION

In this paper, we investigate the magnetohydrodynamic (MHD) dynamo by a thermal convection motion of plasma in the geometry of a rotating spherical shell, such as a stellar convection zone. Our model would be appropriate for solar-type stars but our present interest is in the understanding of general MHD dynamo physics, rather than a direct comparison with a special star. Many dynamo studies focus on the so-called α-effect [1–3]. This is reasonable since an essential process of the field generation is extracted in the α-effect. It should be stressed, however, that the studies of the α-effect is physically inconsistent unless it is proven that the convection motion driven by thermal energy naturally have a flow pattern which produces the α-effect. In this paper, time developments of thermal convection motion as well as the magnetic field are self-consistently calculated. The solved equations are the full-set of the MHD equations. There is no explicit α-effect term in the induction equation. We have reported in previous papers that a strong magnetic field, whose energy become greater than convection energy, is generated [4], and a dominant dipole magnetic field is spontaneously generated [5]. In this paper, we present a physical mechanism of how the dipole field is generated.

II. MODEL AND METHOD

We set up a simulation model as simple as possible since our present purpose is to understand the fundamental process of the MHD dynamo. Suggested by stellar convection zone, we consider a spherical shell geometry (see Fig. 1a). The system consists of an inner spherical core that has a heat source to keep its surface ($r = r_i$) at a high temperature, an outer heat absorbing spherical boundary surface ($r = r_o$) that is kept at a low temperature, and an intermediate conductive fluid medium sandwiched by the two spherical boundaries ($r = r_i$ and r_o). The conductive medium is represented by the MHD equations with gravity force. The calculation is implemented on a spherical coordinate (r, ϑ, φ) grid point system with a finite difference method [4,6].

Simulations are performed in a full spherical shell region ($r_i \leq r \leq r_o, 0 \leq \vartheta \leq \pi, 0 \leq \varphi \leq 2\pi$). The grid numbers $(N_r, N_\vartheta, N_\varphi)$ are chosen to be $(50, 38, 64)$. The boundary conditions at $r = r_i$ and r_o are such that $\mathbf{v} = 0$ and $E_r = \partial E_\vartheta / \partial r = \partial E_\varphi / \partial r = 0$. This means that the magnetic field has only radial components on the boundaries ($B_r \neq 0$, $B_\vartheta = B_\varphi = 0$) [4,7]. This boundary condition is proper for solar dynamo problem since it is observed that the magnetic field at the photosphere is always perpendicular to the surface [7]. This boundary condition guarantees the poynting flux $\mathbf{E} \times \mathbf{B}$ through the boundary to be zero since the vector $\mathbf{E} \times \mathbf{B}$ has no radial component. Therefore, we can definitely say that strong magnetic field in the spherical shell obtained at the end of this simulation is a result of an MHD dynamo process, not an artificial or numerical inflow of magnetic energy through the boundaries.

The parameters used in this simulation are as follows: $r_i = 0.3$, $r_o = 1.0$, $R = 1 \times 10^4$, $\eta = 2.7 \times 10^{-4}$, $T = 5.88 \times 10^6$, $Pr = 1$, $Pr_m = 10.6$, where R, η, T, Pr, Pr_m are Rayleigh number, nondimensional resistivity normalized by $\mu_0 c_s r_o$ (c_s is sound speed), Taylor number, Prandtl number, Magnetic Prandtl number, respectively. These parameters are defined as follows: $R = g(\beta c_p - g)(r_o - r_i)^4/(\kappa\nu)$, $T = (2\Omega(r_o - r_i)^2/\nu)^2$, $Pr = \nu/\kappa$, $Pr_m = \nu/\eta$, where g=gravity acceleration, β=temperature gradient coefficient, (Initial temperature profile is given by $\beta/r + const.$) c_p=specific heat with constant pressure, κ=thermal conductivity, ν=viscosity, and Ω=rotation angular velocity of the spherical shell. Although our purpose of this paper is not to simulate the sun or other specific star, it would be helpful to show various values adopted in this simulation in dimensional form. If we take the outer radius r_o, mass density $\rho(r_o)$, and temperature $T(r_o)$ as the solar values [8] ($r_o = 6.7 \times 10^8(m)$, $\rho(r_o) = 8 \times 10^{-5}(kgm^{-3})$, and $T(r_o) = 6.6 \times 10^3(K)$), other dimensional values can be calculated as, for example, heat flux $= 1.1 \times 10^5(J/s \cdot m^2)$, gravity acceleration $= 4.1(m/s^2)$, viscosity $\nu = 1.1 \times 10^6(kg/m \cdot s)$, thermal conductivity $\kappa = 1.4 \times 10^{10}(W/m^3)$, resistivity $\eta = 1.7 \times 10^3(\Omega/m^3)$. Some of these values are quite different from those of the sun. Especially, the last three dissipation coefficients are apparently too high for high temperature plasma. This means that we simulate an MHD dynamo in a system of strong dissipation limit.

Time development of the difference MHD equations are calculated by the 4th-order Runge-Kutta method [9]. Time is normalized by sound crossing time ($=r_o/c_s$). In this normalization, the thermal diffusion time τ_{th}, viscous diffusion time τ_{vis} and resistive diffusion time τ_{res} are given, respectively, by $\tau_{th} = \tau_{vis} = 240$ and $\tau_{res} = 3700$. The simulation is made until $t = 5500$, that is about 23 τ_{th} (τ_{vis}) or 1.5 τ_{res}. The sphere rotates about 6130 times in this period. The turnover time of the convection motion is roughly ten times of the rotation period of the sphere.

III. RESULTS

A. Structure of Convection Motion

The initial condition is given by a hydrostatic and thermal equilibrium state with no magnetic field. A thermal convection instability, with no magnetic field, grows when a weak random noise is superimposed upon the initial temperature profile. Thermal convection in a rotating spherical shell has been investigated by theory [10,11] and numerical simulation [12–15,6,16]. In our calculation, the convection reaches a saturated state at $t = 150$. The saturated convection motion is non-turbulent and has almost no temporal fluctuation. The convection pattern slowly drifts westward. Well-organized anticyclonic and cyclonic columnar cells, or, anticyclonic and cyclonic convection columns, whose axes are parallel to the rotation axis (z-axis), are formed in pairs (side by side) and encircle the rotation axis (see Fig. 1b). The

formation of the straight convection columns are due to the Taylor-Proudman theorem [17]. It is known that there is another constraint of an MHD fluid in a rotating system which is found by J.B. Taylor [18]. However, the J.B. Taylor's constraint is not satisfied in our simulation since the necessary condition for this constraint (negligibly small viscosity and very slow flow) is not satisfied in our case.

The fluid in a cyclonic (anticyclonic) column rotates in the same (opposite) direction as the rotation of the spherical shell. The columns have negative (positive) helicity, $\mathbf{v} \cdot \omega$, in the northern (southern) hemisphere due to the axial, or z-, flow component in each column which is directed toward (away from) the equator in the cyclonic (anticyclonic) columns. This axial flow induces horizontally converging, or sucking, flow near the outer boundary at both (northern and southern) ends of the cyclonic columns. This horizontal converging flow plays an important role in the dipole field generation which will be explained later on. Effects of compressibility on the convection dynamics are weak in this calculation since the maximum speed of the convection velocity is about 10% of the sound velocity.

B. Magnetic Field Generation

After the convection motion has reached to the saturated state (at $t = 256$), we superimpose a weak seed of random magnetic field. The seed field is given by curl of the following vector potential having only the radial component; $A_r = \sin((r-r_i)\pi/(r_o-r_i)) \times F(\vartheta, \varphi)$, where the function F is a random field with small amplitude: The value of F on each grid point is determined by a random number generator between 0 and 0.001. The amplitude of the initial magnetic energy induced from this vector potential is only 1.61×10^{-3} of the convection kinetic energy. Although the initial magnetic field has a complicated structure, we get a simple magnetic field structure at the end.

After a short while, the magnetic energy starts growing exponentially. The magnetic energy grows beyond the kinetic energy at about $t = 4000$ and saturates at an energy level about two times larger than the kinetic energy in the present case. Both energies have no appreciable temporal variations in the final state. The convection motion in the final state is non-turbulent and keeps its well-organized structure. One of interesting findings of this simulation is that in spite of the existence of such a strong magnetic field, the columnar structure of the convection motion is not destroyed. This can be explained by the fact that the generated magnetic field is nearly force-free ($\mathbf{J} \times \mathbf{B} \sim 0$) in the most part.

C. Structure of Magnetic Field

In order to understand the generation mechanism of the magnetic field, we examine in detail the magnetic field structure in the shell at $t = 3400$ when the magnetic energy is exponentially growing. It is found that dividing the magnetic field into toroidal and poloidal parts helps understanding the field

structure. The blue lines in Fig. 2 show the toroidal field lines. Fig. 2(a) to (d) show four different views. There are 12 field lines in Fig. 2 (6 in each hemisphere) which are all traced for length of 17.14 (in the unit of r_o) though the field lines can be traced much more. The grey transparent bar-like objects are isosurfaces of positive z-component of vorticity ω_z which stands for cyclonic convection columns. There is a strong toroidal magnetic fluxes in each hemisphere. The polarity of these toroidal fluxes is antisymmetric about the equator; westward in the northern hemisphere and eastward in the southern hemisphere. An interesting feature of the toroidal field is that the shape of the lines viewed from north (Fig. 2(a)) is like a flower with six petals. It will be shown that this characteristic shape of the lines is a key to understand the generation mechanism of the magnetic field.

Green and red lines in Fig. 3 show poloidal field lines in the spherical shell. All the lines are traced from the outer boundary ($r = r_o$). The starting points of the lines are chosen so that the magnetic field strength $|B|$ at the points are greater than 50% of maximum value $|B|_{max}$ on the outer boundary. In contrast to the toroidal field lines (Fig. 2), the poloidal field lines (Fig. 3) cannot be traced long since they soon reach the spherical boundaries. The lines are colored due to the position of each line's end point. The end point of a red line is on the inner boundary. In other words, the red lines connect two points one of which is on the outer boundary and the other is on the inner boundary. On the other hand, the end point of a green line is on the outer boundary: Green lines connect two points which are both on the outer boundary. A distinct feature of Fig. 3 is that all the field lines near the outer boundary are converged in the six cyclonic columns. The convergence mechanism will be explained later on.

Spontaneously generated magnetic field on the outer boundary $B_r(r = r_o)$ is expanded by spherical harmonics $Y_l^m(\vartheta, \varphi)$; $B_r(r_o) = \sum_{\ell=1} \sum_{m=-\ell}^{\ell} a_l^m Y_l^m$. On comparing powers of each mode, we find that the most strongly excited mode is the dipole moment ($\ell = 1, m = 0$). In the final state ($t = 5500$), $|a_1^0|^2 = 3.4 \times 10^{-4}$. The second moment is the octapole: $|a_3^0|^2 = 2.0 \times 10^{-4}$. The third one is non-axisymmetric moment ($\ell = 7, m = \pm 6$), $|a_7^6|^2 + |a_7^{-6}|^2 = 1.4 \times 10^{-4}$. (Azimuthal mode number $|m| = 6$ comes from six pairs of convection columns; see Fig. 1b.) The quadrupole ($\ell = 2, m = 0$) is very weak: $|a_2^0|^2 = 6.8 \times 10^{-6}$. All these numbers stay same levels after the dynamo saturation. More generally, the moments with the quadrupole symmetry ($\ell + m =$ even) remain at a very low amplitude compared with the moments with dipole symmetry ($\ell + m =$ odd). Here the dipole symmetry means that $B_r(\vartheta) = -B_r(\pi - \vartheta)$, $B_\vartheta(\vartheta) = B_\vartheta(\pi - \vartheta)$, and $B_\varphi(\vartheta) = B_\varphi(\pi - \vartheta)$. On the other hand, the quadrupole symmetry means that all signs in the right hand side of the above equations are opposite.

In Fig. 4a, azimuthally-averaged poloidal magnetic components are shown by thick solid lines (yellow) and intensities of toroidal components are color plotted: Red (blue) denotes westward (eastward) toroidal field. Illustrated in Fig. 4b is a three-dimensional structure of magnetic field lines of the potential field at a final state ($t = 5500$). Each line is colored in order to show the direction of the magnetic field (blue $\rightarrow$ green $\rightarrow$ red). It is obviously seen in Fig. 4a and 4b that the magnetic field with the dipole symmetry

is strongly excited.

D. Generation Mechanism of Dipole Field

Let us now go on to the generation mechanism of the dipole field. We pay attention to a pair of cyclonic and anticyclonic columns in the northern hemisphere (see Fig. 5a). Suppose that there is a westward toroidal magnetic field line encircling convection columns in the northern hemisphere at the middle latitude (line 1 in Fig. 5a). Because of the rotating motion of each column, the field line is swallowed up in the valley of anticyclonic and cyclonic columns (cyclonic in the west, anticyclonic in the east), namely, toward the inner sphere (line 2). This stretches the field line against the field tension force ($-\mathbf{v}\cdot\mathbf{J}\times\mathbf{B} > 0$; positive dynamo). Simultaneously, the axial flow, or z-component flow in the columns pulls up the sheared line and generates z-, or poloidal, component of the magnetic field (line 3). The same process takes place in the southern hemisphere, too. The generated field line configuration in the northern and southern hemispheres is deformed as shown in Fig. 5b, since the toroidal component is antisymmetric about the equator (see the color in Fig. 4a). Then, the field lines in both hemispheres reconnect with each other on the equatorial plane at points a, a', a'', ... in Fig.5b. Field line reconnection leads to the formation of six poloidal field lines as shown in Fig. 5c since there are six pairs of cyclonic and anti-cyclonic convection columns.

Fig. 6 shows that the above process is certainly taking place in our simulation. An magnetic field line at $t = 3400$ (the same data as Fig. 2 and 3) is shown in Fig. 6. The field line is colored depending on the value of the dynamo term $-\mathbf{v}\cdot(\mathbf{J}\times\mathbf{B})$ at each point on the line. The line becomes red where the term is large positive. In other words, a strong dynamo action is taking place in regions where the field line is red. The white arrows on the line stand for the strength and direction of the flow velocity at the points. Semi-transparent bar-like objects are convection columns visualized by isosurfaces of $\omega_z = \pm 0.6$. The blue ($\omega = 0.6$) one denotes a cyclonic convection column and the pink ($\omega = -0.6$) one denotes an anticyclonic column. We can intuitively understand from Fig. 6 how the poloidal component is generated by the deformation of the field line. And the arrows indicate that the inward flows between the columns are in the opposite direction of the field line's tension force. Therefore, $-\mathbf{v}\cdot\mathbf{J}\times\mathbf{B}$ becomes positive there which means that the magnetic energy is generated at those points. Glatzmaier and Roberts [19,20] have also shown that a dipole field is generated by the MHD convection in a rotating spherical shell. The dynamo mechanism of their simulation is quite different from ours because of the very different parameter range.

It should be noted here that the above process of the poloidal field generation can be understood as an α-effect. The negative (positive) helicity in the northern (southern) hemisphere generates parallel (antiparallel) current to the toroidal magnetic field. (But note that this α-effect is self-consistently

induced by non-turbulent MHD convection.) The α-effect was first postulated by Parker in 1955 [1]. Many numerical simulations have been performed on the magnetic field generation due to the α-effect in spherical geometries [21–24]. In these studies, the existence of the α-effect in the induction equation of the magnetic field is explicitly supposed and distribution and amplitude of the α-term are arbitrarily given. The most important point in this simulation is that the α-effect appeared in our calculation is self-consistently generated from the MHD convection motion.

We also point out a similarity between the above explained dipole field generation process and a field-reversed configuration (FRC) formation process in plasma experiments. It is know from both laboratory [25,26] and numerical [27] experiments that when two spheromaks collide head on, they are merged together and an isolated plasma with singly connected flux surfaces is formed. The resultant field configuration is an FRC when the two spheromaks have opposite sings of the magnetic helicity. Anti-parallel toroidal fields in each spheromak are canceled each other after the merging and a purely poloidal field is left. The poloidal field generation observed in this dynamo simulation is similar to this FRC formation by merging of two spheromaks. The two spheromaks correspond to two toroidal fluxes in the northern and the southern hemispheres (see Fig. 2).

Distribution of the radial magnetic field in the final state ($t = 5500$) at the outer boundary $B_r(r = r_o)$ viewed from the north is shown in Fig. 7. The view from the south is the same due to the symmetry. The central circle denotes the inner boundary. The six solid thick lines show the loci of cyclonic columns on a spherical plane at $r = 0.9$, specifically, the iso-lines of positive z-vorticity ω_z (at the level of 50 % of its maximum value). There are six spots of strong B_r flux region (thin contours) whose locations coincide with those of the cyclonic columns. This figure indicates that the magnetic fluxes are accumulated, with equal intensity and polarity, in all the cyclonic columns near the outer boundary. This flux concentration effect is caused by the horizontal converging flow in the cyclonic columns near the outer boundary. The converging flow collects the radial magnetic flux in the cyclonic columns. The flux concentration within the columns is also observed near the equatorial plane and is described in detail in our previous paper [4]. It should be noted that the magnetic flux concentration is observed in the geomagnetic field [28].

E. Toroidal Field Generation Process

We have presented generation mechanism of the poloidal field in Fig. 5. Understanding of the dynamo mechanism is completed when we present how the toroidal field is converted from the poloidal field. The conversion mechanism is not surprising: It is a well-known ω-effect. Fig. 8 shows profiles of differential rotation and the convection columns. Thin solid and dashed lines are contours of $\overline{v}_\varphi$ (azimuthally averaged v_φ). The solid (dashed) lines denote eastward (westward) mean flow. The thick solid line shows the contour line of $\omega_z = 0.6$ in a meridian cross section which stands for the location of a cyclonic

columns in this meridian plane. Since the poloidal field is generated in the convection columns, we should focus on the region inside of the thick line in Fig. 8. We can see that there is a westward mean flow in the equatorial plane at the position of the convection columns. This westward mean flow seems to be a persistent character in the thermal convection in rapidly rotating spherical shells. It is observed in our previous paper [6] and other simulations (see, for example, figure 3 in a paper by Sun and Schubert [16]). The poloidal field lines threading through the equatorial plane from north to south are deformed or drawn by this westward mean flow in the equatorial plane. Therefore, toroidal (east-west) component of the magnetic field is born by this differential rotation; westward in the northern hemisphere and eastward in the southern hemisphere.

The above process of the toroidal field generation by the differential rotation is called ω-effect [2]. An interesting point in this simulation is that the kinetic energy of the differential rotation is only 6% of the total kinetic energy. Therefore, it should be confirmed that the toroidal field is certainly generated by such a relatively weak differential rotation. For that purpose, we have shown that the magnetic field decays if the differential rotation component is removed from the velocity field. We can take the kinematic dynamo approach in this proof since we are interested only in the magnetic field amplification process, not in the feedback process. In a kinematic dynamo study, time development of the magnetic field is investigated under a fixed velocity field $\mathbf{v}^*$. Here, the velocity $\mathbf{v}^*$ is determined as follows: First, we take the velocity field $\mathbf{v}^o$ from the self-consistent dynamic simulation explained so far in this paper. The data $\mathbf{v}^o$ is taken at $t = 256$ when the convection has already reached to the saturated state. Then, the axisymmetric component of the longitudinal velocity $\overline{v}_\varphi$, is removed from $\mathbf{v}^o$; $\mathbf{v}^* = \mathbf{v}^o - \overline{v}_\varphi \hat{\varphi}$. From this definition, the velocity field $\mathbf{v}^*$ has exactly no differential rotation. Since $\overline{v}_\varphi$ is weak, the velocity field $\mathbf{v}^*$ is very similar to that of $\mathbf{v}^o$. There are six pairs of cyclonic and anticyclonic convection columns in this case, too. The helical flow pattern in each column, which is the origin of the α-effect, is the same as that of $\mathbf{v}^o$. A random weak magnetic field is seeded into this velocity field $\mathbf{v}^*$. Then, it is found that the seed field decays under the fixed velocity $\mathbf{v}^*$. So, there is no dynamo in the absence the differential rotation. For a comparison, the velocity field $\mathbf{v}^*$ is replaced with the original velocity $\mathbf{v}^o$. In this case, the seed magnetic field is amplified. The growing magnetic field has the same structure as that of the self-consistent dynamic simulation in its early linear phase before the saturation (Fig. 2 and 3). This is a matter of course since, in the early phase, the growing magnetic is so weak that the $\mathbf{J} \times \mathbf{B}$ force is negligibly small and, therefore, the time development of the magnetic field is essentially kinematic. The above numerical experiments clearly demonstrates that the differential rotation is an indispensable factor for the whole dynamo cycle.

IV. SUMMARY

In summary, we have shown that a dipole magnetic field is spontaneously generated by an MHD thermal convection in a rotating spherical shell. Structure and the generation mechanism of the magnetic field is examined in detail. The poloidal field is generated when toroidal field lines are stretched and deformed by inward flows between cyclonic and anticyclonic convection columns. This process can be understood as an α-effect. The generated poloidal field is concentrated in cyclonic convection columns near the outer boundary because of the horizontal convergent flow in the cyclonic columns. Toroidal field is generated from the poloidal field by the westward mean flow in the equator. We can conclude from this simulation that the dipole field generation is a natural consequence arising from the columnar convection structure in the rotating spherical geometry.

ACKNOWLEDGMENTS

The authors would like to thank Complexity Simulation Group of Theory and Computer Simulation Center, National Institute for Fusion Science for helpful discussion. This work is supported by Grant-in-Aid from the Ministry of Education, Science and Culture in Japan.

---

[1] E.N. Parker, *Astrophys. J.*, **122**, 293-314, 1955

[2] H.K. Moffatt, *Magnetic Field Generation in Electrically Conducting Fluids*, Cambridge University Press, London, 1978

[3] F. Krause, and K.H. Radler, *Mean Field Magnetohydrodynamics and Dynamo Theory*, Pergamon Press, Oxford, 1980

[4] A. Kageyama, T. Sato, and the Complexity Simulation Group, *Phys. Plasmas*, **2**, 1421-1431, 1995

[5] A. Kageyama, T. Sato, and the Complexity Simulation Group, *Research Report NIFS*, **NIFS-359**, 1995

[6] A. Kageyama, T. Sato, and K. Watanabe, *Phys. Fluids B*, **5**, 2793-2805, 1993

[7] P.A. Gilman, and J. Miller, *Astrophys. J. Suppl.*, **46**, 211-238, 1981

[8] M. Stix, *The Sun*, corrected 2nd printing, p. 47 Springer-Verlag, New York, 1991

[9] W.H. Press, S.A. Teukolsky, W.T. Vetterling, and B.P. Flannery ed, *Numerical Recipes in C*, second edition, p. 710, Cambridge University Press, New York, 1992

[10] P.H. Roberts, *Phil. Trans. R. Soc. London Ser.*, **A263**, 93-117, 1968

[11] F.H. Busse, *J. Fluid Mech.*, **44**, 441-460, 1970

[12] P.A. Gilman*Solar Phys.*, **27**, 3-26, 1972

[13] G.A. Glatzmaier and P.A. Gilman, *Astrophys. J. Suppl.*, **45**, 351-380, 1981

[14] P.A. Gilman, and J. Miller, *Astrophys. J. Suppl.*, **61**, 585-608, 1986

[15] K.-K. Zhang, *J. Fluid Mech.*, **236**, 535-556, 1992

[16] Z.-P. Sun and G. Schubert, *Phys. Fluids*, **7**, 2686-2699, 1995

[17] S. Chandrasekhar, *Hydrodynamic and Hydromagnetic Stability*, Dover, New York, 1961

[18] J. B. Taylor, *Proc. Roy. Soc.*, **A274**, 274, 1963

[19] G. A. Glatzmaier, and P. H. Roberts, *Phys. Earth and Planet. Inter.*, **91**, 63-75, 1995

[20] G.A. Glatzmaier, P.H. Roberts, *Nature*, **377**, 203-208, 1995

[21] P.H. Roberts, *Phil. Trans. R. Soc. London Ser.*, **A 272**, 663-703, 1972

[22] P.H. Roberts, and M. Stix, *Astron. & Astrophys.*, **18**, 453, 1972

[23] S. A. Jepps, *J. Fluid Mecha.*, **67**, 625, 1975

[24] W. P. Wood, and H. K. Moffatt, *Geophys. Astrophys. Fluid Dynamics*, **32**, 135-161, 1985

[25] M. Yamada, Y. Ono, A. Hayakawa, M. Katsurai, and F. W. Perkins, *Phys. Rev. Lett.*, **65**, 721-724, 1990

[26] Y. Ono, A. Morita, M. Katsurai, and M. Yamada, *Phys. Fluids*, **B5**, 3691–3701, 1993

[27] T.H. Watanabe, T. Sato, T. Hayashi, and K. Watanabe, *J. of Plasma and Fusion Research*, in Japanese, **72**, 249-258, 1996

[28] D. Gubbins, and J. Bloxham, *Nature*, *Nature*, **325**, 509–511, 1987

Figure Captions

FIG. 1. (Color) Simulation model and convection cells. (a) The interior of the model is exposed by cutting a piece of the sphere. The green part represents the equatorial plane and the yellow does two meridional planes. The meshes indicated in these planes illustrate how the system is implemented on a grid point system. The number of the grids shown here does not represent the actual one but is reduced for brevity. An electrically conducting fluid is sandwiched by two concentric spheres with different temperatures; hot (red) and cold (violet). The system is rotating with a constant angular velocity as shown by arrows. (b) Well-organized columnar convection cells (convection columns) obtained by the simulation with no magnetic field. These are visualized by isosurfaces of axial component of vorticity, ω_z. The cyclonic columns (green) and anti-cyclonic columns (yellow) appear in an alternate way to encircle the rotation axis.

FIG. 2. (Color) Toroidal magnetic field structure. Toroidal field lines (blue) are traced at $t = 3400$ when the magnetic energy is exponentially growing. The four panels (a) to (d) are views from four different angles. (a) is from the north and (d) is from the equator. The semi-transparent grey bar-like objects are cyclonic convection columns visualized by isosurfaces of vorticity ω_z.

FIG. 3. (Color) Poloidal magnetic field structure. Poloidal field lines (red and green) are traced at $t = 3400$ when the magnetic energy is exponentially growing. The four panels (a) to (d) are views from four different angles. (a) is from the north and (d) is from the equator. The semi-transparent grey bar-like objects are cyclonic convection columns visualized by isosurfaces of vorticity ω_z. All the field lines are traced from the outer spherical boundary. The lines are colored depending on the end point of each line: The red lines end at the inner boundary and the green lines end at the outer boundary.

FIG. 4. (Color) Dipole field generation. (a) The three panels show three time sequential color plots of the azimuthally-averaged meridional (poloidal) component of the generated magnetic field in a meridian plane (yellow). The number of lines represents the intensity of the field. The bright disc-like region represents the simulation region where the innermost part is the hot temperature boundary and the outermost is the low temperature boundary. The reddish part is the color contour of the averaged westward toroidal field and the bluish is that of the eastward one. One can confirm from these color plots that the dipole-dominant field originates from the pair of the westward (northern hemisphere) and eastward (southern hemisphere) components of the toroidal field. (b) Three-dimensional view of magnetic field lines of the potential field emerged through the outer spherical boundary from the convection columns at the final state ($t = 5500$). Each magnetic field line is colored in order to show the direction of the magnetic field (blue $\rightarrow$ green $\rightarrow$ red). One can clearly see that the dipole field is preferentially generated.

FIG. 5. Dynamo mechanism. (a) Schematic diagram of the dipole field generation mechanism. A pair of cyclonic column (west) and anticyclonic column (east) and magnetic field lines in the northern hemisphere are shown. The magnetic field line 1 encircle the convection columns. The lines are swallowed up toward the inner sphere at the boundary region between cyclonic and anticyclonic columns because of the rotating motion of the columns (denoted by white horizontal big arrows). (On the other hand, the field lines are pushed out at the anticyclonic (west)-cyclonic (east) boundary.) Axial, or z-, component flows in the columns (denoted by vertical white big arrows) shear the field line so as to generate the southward component of the magnetic field (line 2 and 3). The field lines are strongly stretched, so that the dynamo, $-\mathbf{v}\cdot\mathbf{J}\times\mathbf{B}$ takes place at this place. (b) The poloidal field generation process from the toroidal field explained in (a) takes place in the southern hemisphere, too. Since the toroidal field in the southern hemisphere is eastward (see Fig. 4a), the generated poloidal lines in both hemispheres reconnect with each other on the equatorial plane at points a, a', a'' etc. (c) Six poloidal field lines are generated since there are six pairs of cyclonic and anticyclonic convection columns (see Fig. 1b).

FIG. 6. (Color) A magnetic field line traced at $t = 3400$. The line is red where the dynamo term $-\mathbf{v}\cdot\mathbf{J}\times\mathbf{B}$ is large positive. The white arrows denote flow velocity vectors at each point on the line. Blue (Pink) semi-transparent bar-like objects are cyclonic (anticyclonic) convection columns.

FIG. 7. Distribution of B_r. Contour lines of radial magnetic field B_r at the outer spherical boundary viewed from the north. The central circle denotes the position of the inner spherical boundary. The six thick lines tangent to the inner boundary show the locations of the cyclonic convection columns. One can see that there are six spots of strong B_r flux (thin contour lines). The locations of these spots exactly coincide with those of the cyclonic columns. This flux concentration effect in the cyclonic columns is explained by the converging horizontal flow near the outer boundary in the cyclonic columns. The axial flow in each column, which is downward (upward) in the cyclonic (anticyclonic) columns in this figure, entails horizontal converging flow in the cyclonic columns. The magnetic flux near the outer boundary concentrates by this converging flow in the cyclonic columns.

FIG. 8. Differential rotation and the profile of a convection column in a meridian plane. Solid and dashed thin lines are contours of azimuthally averaged velocity of east-west component ($\overline{v}_\varphi$). The dashed lines stand for negative component, i.e., westward mean flow. The thick solid line is a profile of a convection column in a meridian plane cross section. There is a westward mean flow in the equatorial plane at the position of convection columns.

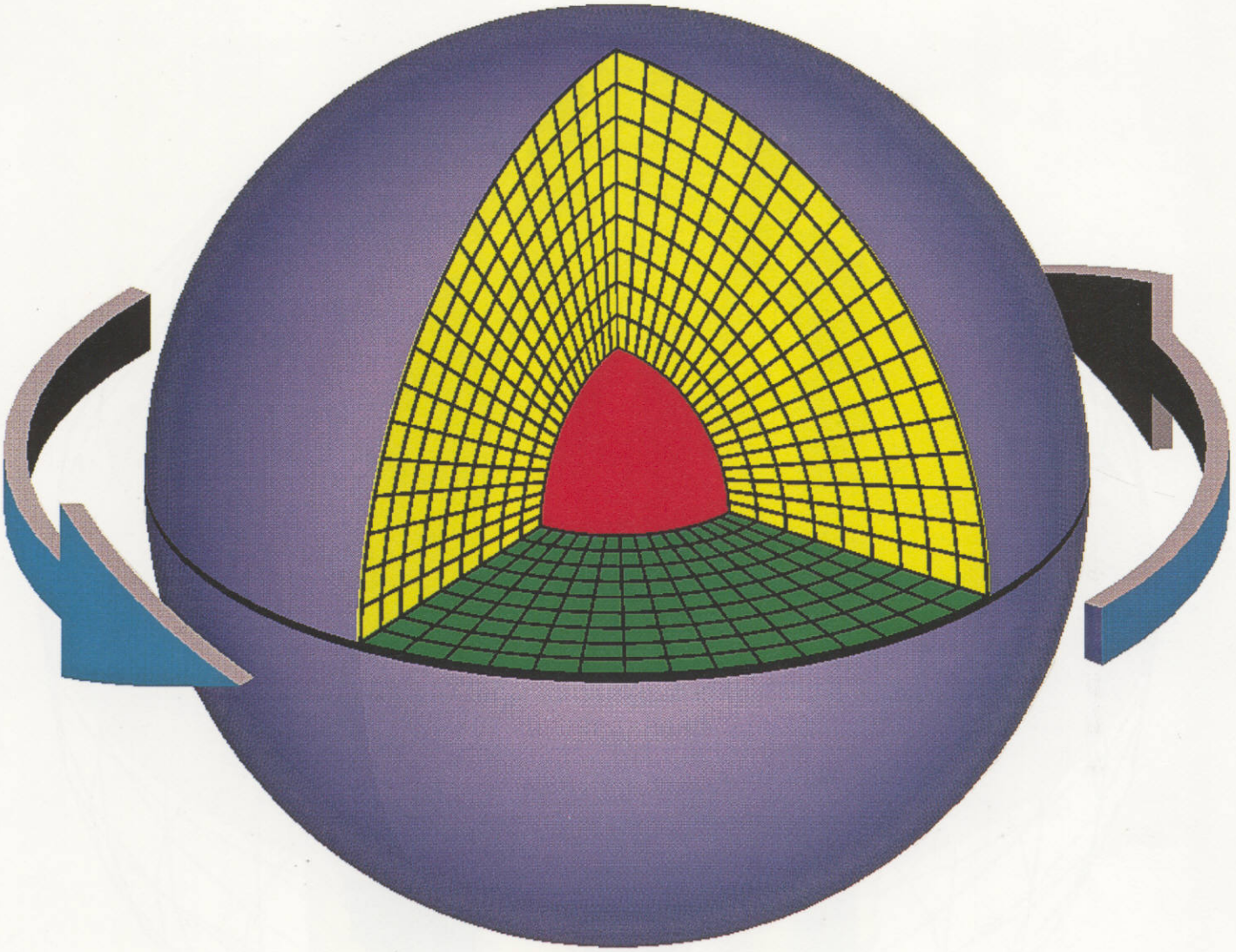

Fig. 1 (a)

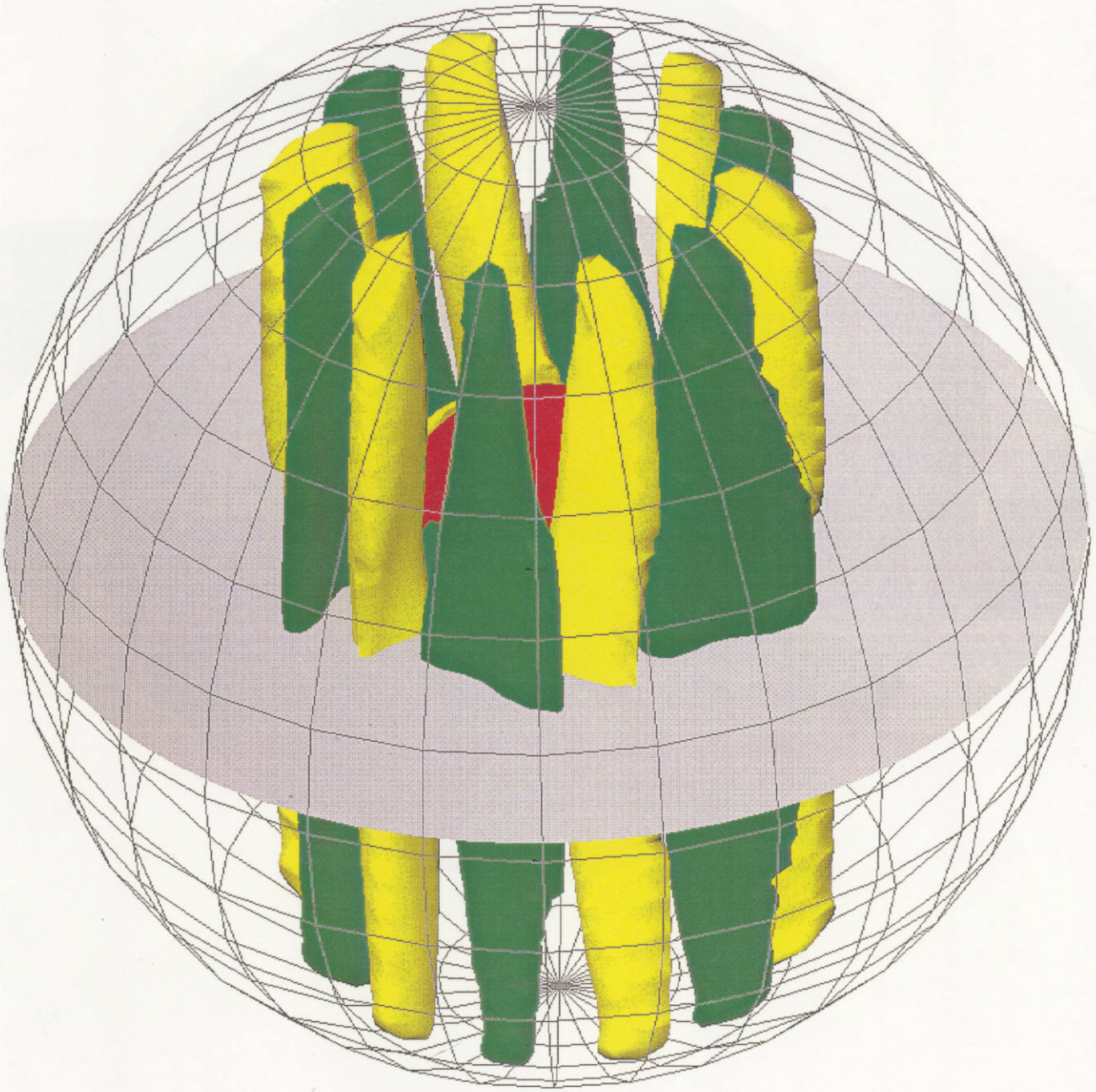

Fig. 1 (b)

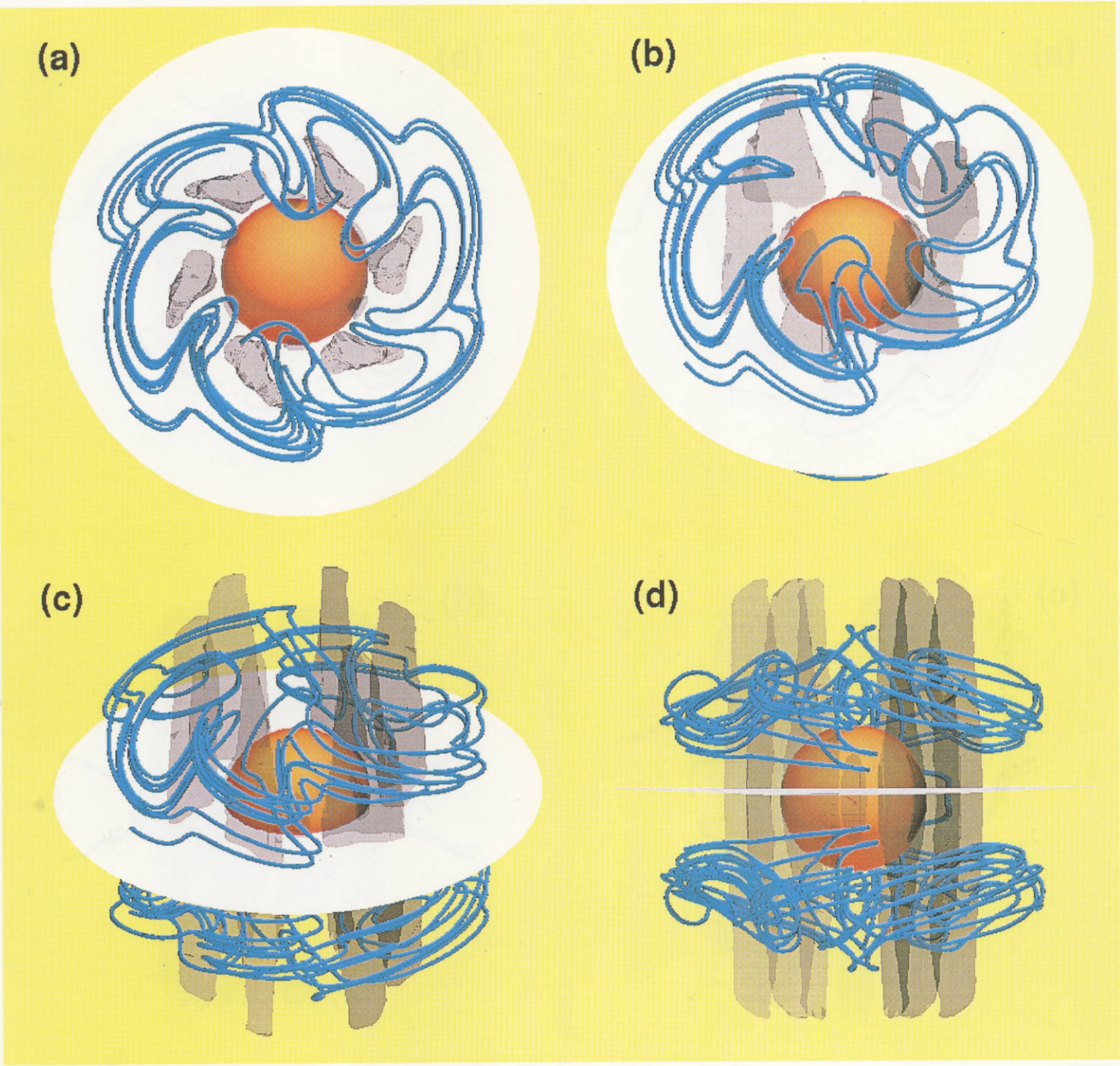

Fig. 2

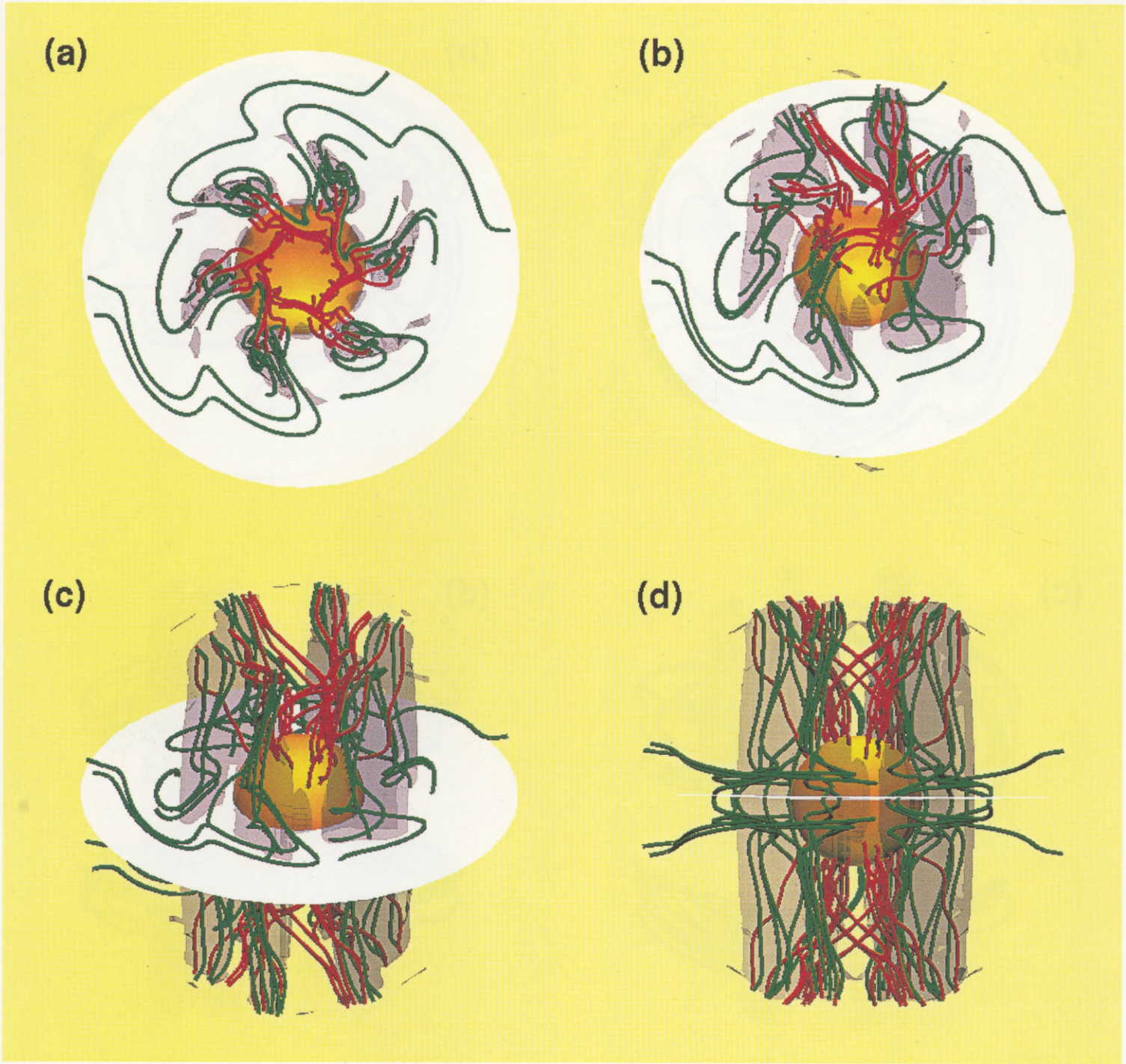

Fig. 3

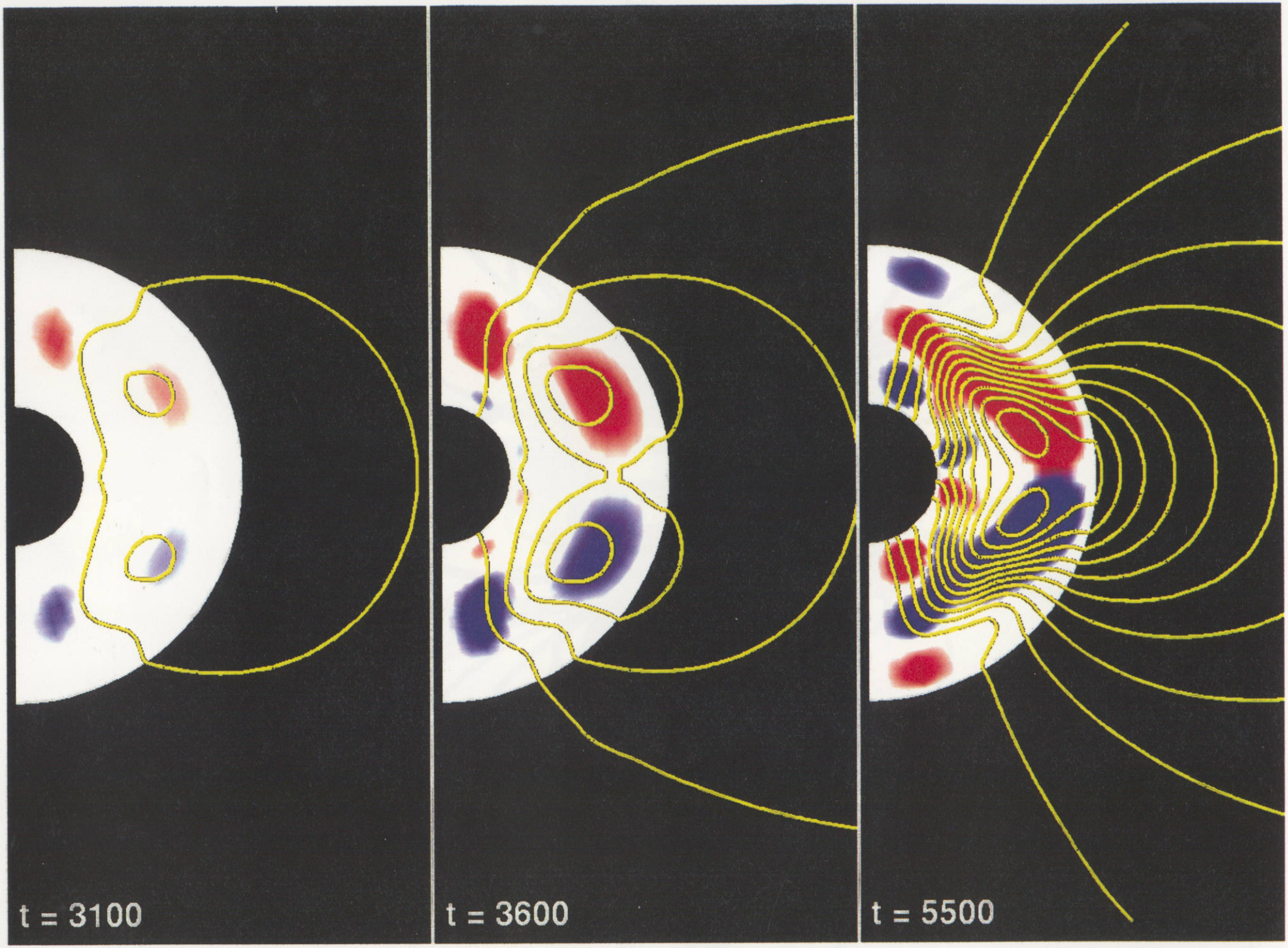

Fig. 4 (a)

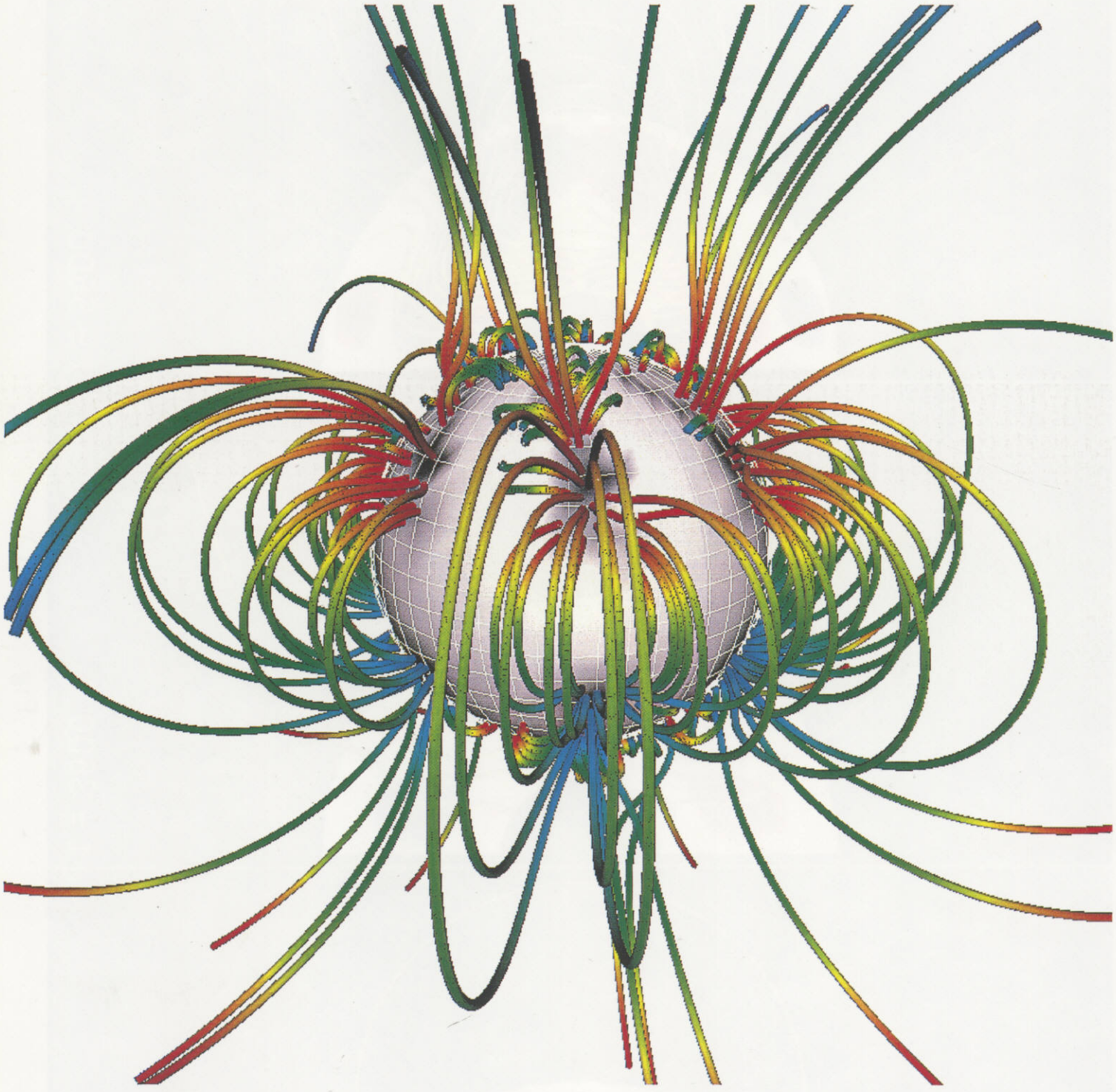

Fig. 4 (b)

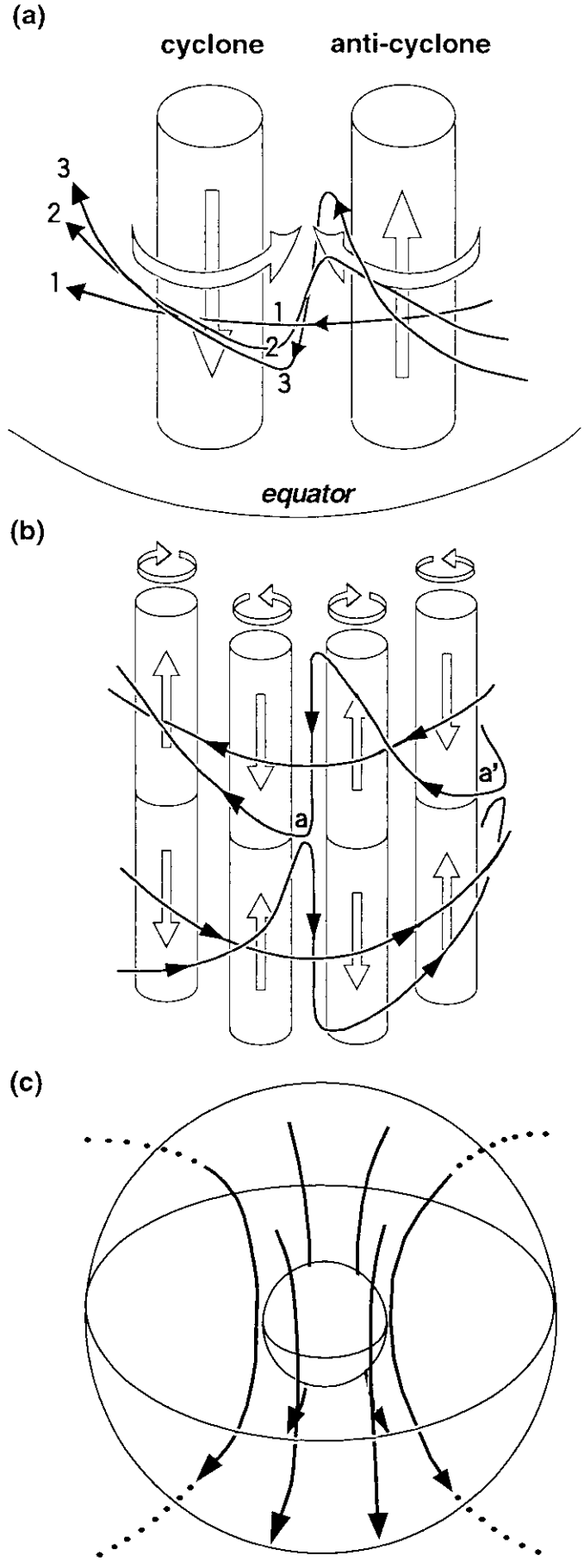

Fig. 5

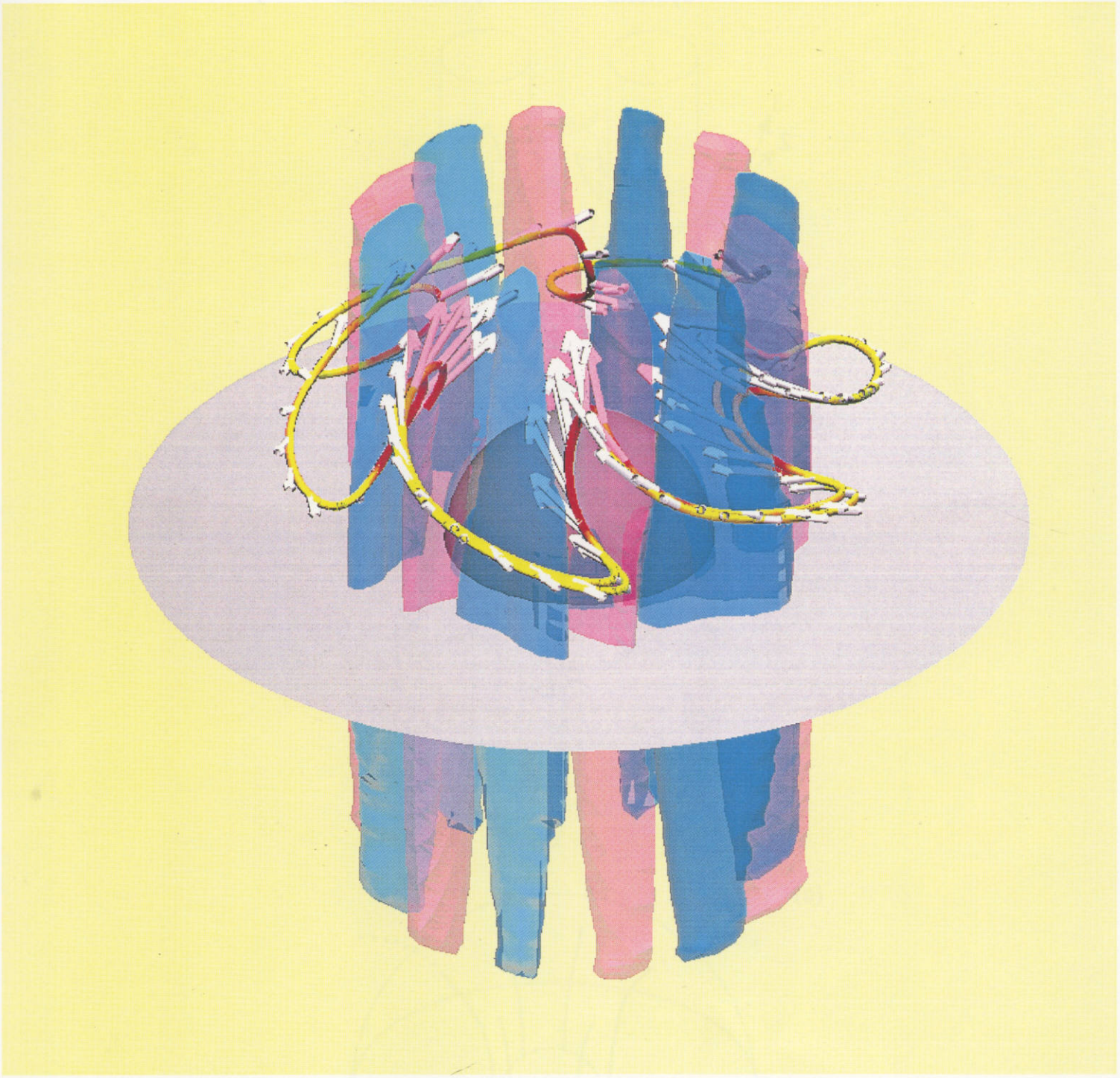

Fig. 6

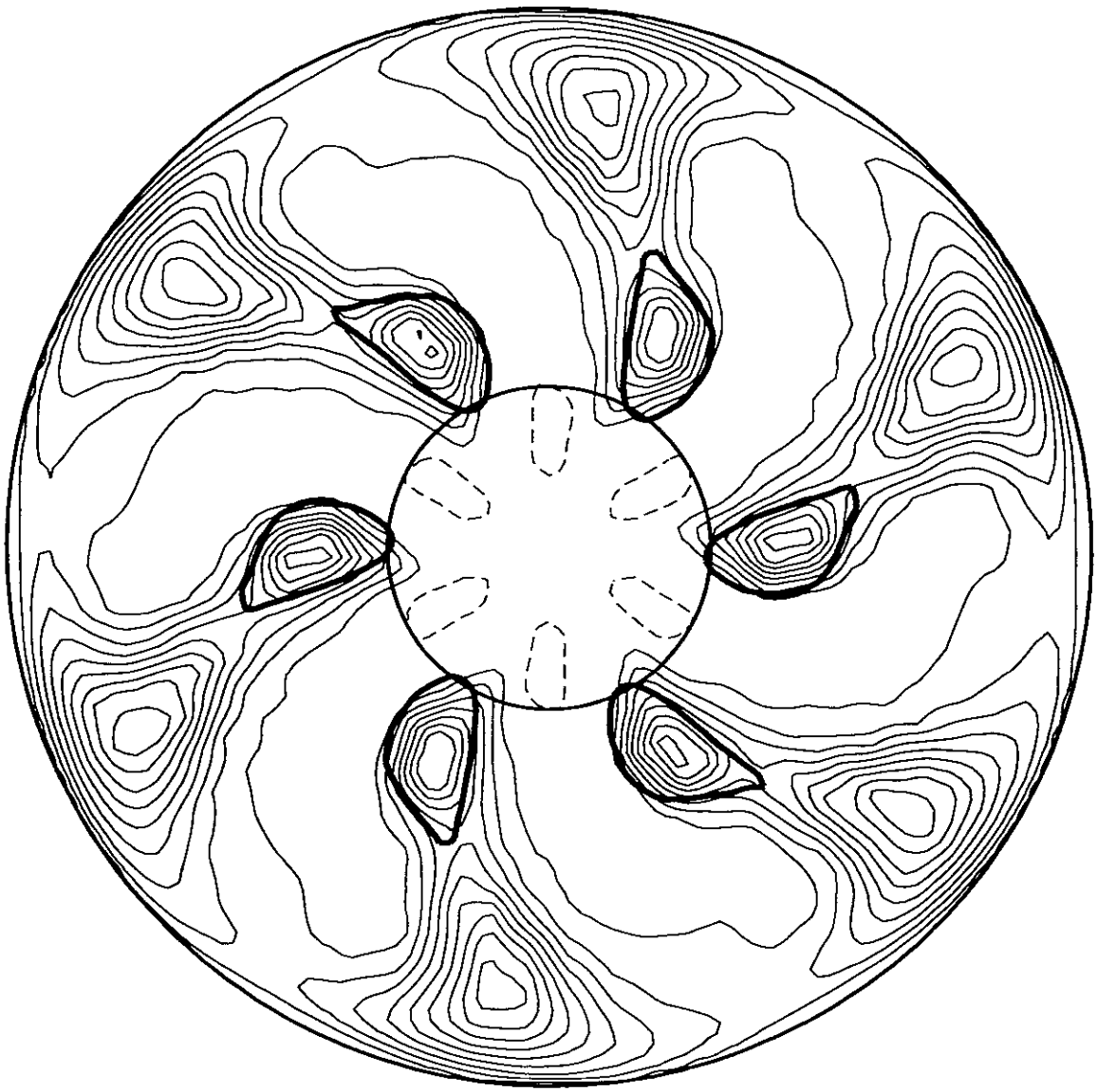

Fig. 7

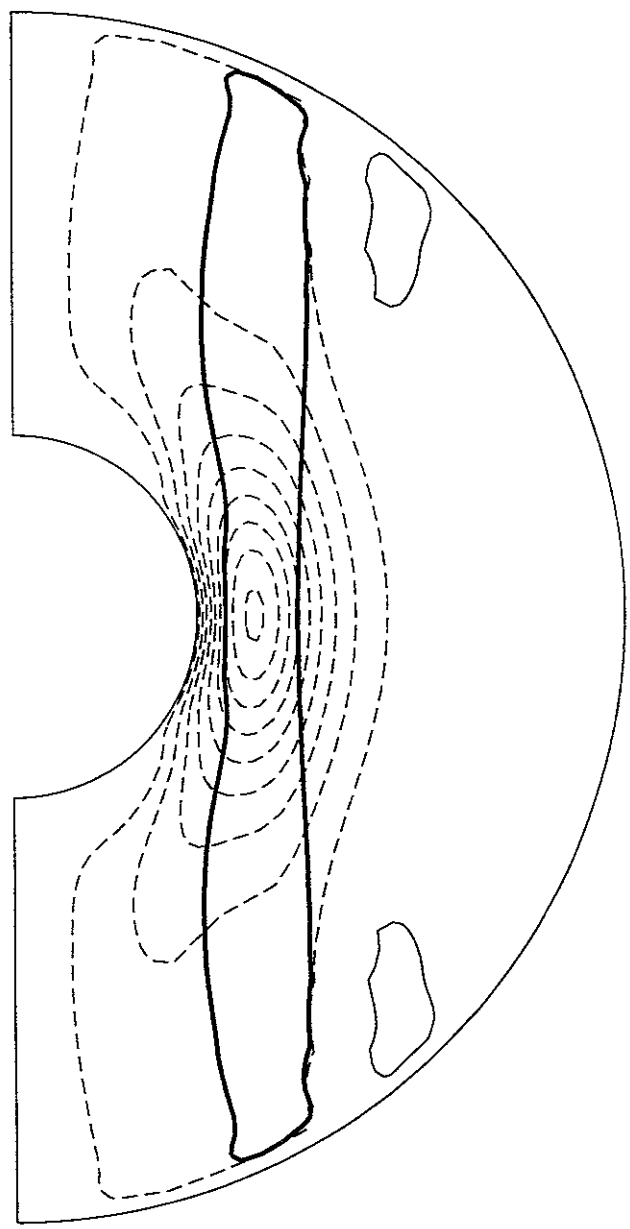

Fig. 8

Recent Issues of NIFS Series

NIFS-421 K. Kondo, K. Ida, C. Christou, V.Yu.Sergeev, K.V.Khlopenkov, S.Sudo, F. Sano, H. Zushi, T. Mizuuchi, S. Besshou, H. Okada, K. Nagasaki, K. Sakamoto, Y. Kurimoto, H. Funaba, T. Hamada, T. Kinoshita, S. Kado, Y. Kanda, T. Okamoto, M. Wakatani and T. Obiki,
Behavior of Pellet Injected Li Ions into Heliotron E Plasmas; July 1996

NIFS-422 Y. Kondoh, M. Yamaguchi and K. Yokozuka,
Simulations of Toroidal Current Drive without External Magnetic Helicity Injection; July 1996

NIFS-423 Joong-San Koog,
Development of an Imaging VUV Monochromator in Normal Incidence Region; July 1996

NIFS-424 K. Orito,
A New Technique Based on the Transformation of Variables for Nonlinear Drift and Rossby Vortices; July 1996

NIFS-425 A. Fujisawa, H. Iguchi, S. Lee, T.P. Crowley, Y. Hamada, H. Sanuki, K. Itoh, S. Kubo, H. Idei, T. Minami, K. Tanaka, K. Ida, S. Nishimura, S. Hidekuma, M. Kojima, C. Takahashi, S. Okamura and K. Matsuoka,
Direct Observation of Potential Profiles with a 200keV Heavy Ion Beam Probe and Evaluation of Loss Cone Structure in Toroidal Helical Plasmas on the Compact Helical System; July 1996

NIFS-426 H. Kitauchi, K. Araki and S. Kida,
Flow Structure of Thermal Convection in a Rotating Spherical Shell; July 1996

NIFS-427 S. Kida and S. Goto,
Lagrangian Direct-interaction Approximation for Homogeneous Isotropic Turbulence; July 1996

NIFS-428 V.Yu. Sergeev, K.V. Khlopenkov, B.V. Kuteev, S. Sudo, K. Kondo, F. Sano, H. Zushi, H. Okada, S. Besshou, T. Mizuuchi, K. Nagasaki, Y. Kurimoto and T. Obiki,
Recent Experiments on Li Pellet Injection into Heliotron E; Aug. 1996

NIFS-429 N. Noda, V. Philipps and R. Neu,
A Review of Recent Experiments on W and High Z Materials as Plasma-Facing Components in Magnetic Fusion Devices; Aug. 1996

NIFS-430 R.L. Tobler, A. Nishimura and J. Yamamoto,
Design-Relevant Mechanical Properties of 316-Type Stainless Steels for Superconducting Magnets; Aug. 1996

NIFS-431 K. Tsuzuki, M. Natsir, N. Inoue, A. Sagara, N. Noda, O. Motojima, T. Mochizuki, T. Hino and T. Yamashina,
Hydrogen Absorption Behavior into Boron Films by Glow Discharges in Hydrogen and Helium; Aug. 1996

NIFS-432 T.-H. Watanabe, T. Sato and T. Hayashi,
Magnetohydrodynamic Simulation on Co- and Counter-helicity Merging of Spheromaks and Driven Magnetic Reconnection; Aug. 1996

NIFS-433 R. Horiuchi and T. Sato,
Particle Simulation Study of Collisionless Driven Reconnection in a Sheared Magnetic Field; Aug. 1996

NIFS-434 Y. Suzuki, K. Kusano and K. Nishikawa,
Three-Dimensional Simulation Study of the Magnetohydrodynamic Relaxation Process in the Solar Corona. II.; Aug. 1996

NIFS-435 H. Sugama and W. Horton,
Transport Processes and Entropy Production in Toroidally Rotating Plasmas with Electrostatic Turbulence; Aug. 1996

NIFS-436 T. Kato, E. Rachlew-Källne, P. Hörling and K.-D Zastrow,
Observations and Modelling of Line Intensity Ratios of OV Multiplet Lines for 2s3s 3S1 - 2s3p 3Pj; Aug. 1996

NIFS-437 T. Morisaki, A. Komori. R. Akiyama, H. Idei, H. Iguchi, N. Inoue, Y. Kawai, S. Kubo, S. Masuzaki, K. Matsuoka, T. Minami, S. Morita, N. Noda, N. Ohyabu, S. Okamura, M. Osakabe, H. Suzuki, K. Tanaka, C. Takahashi, H. Yamada, I. Yamada and O. Motojima,
Experimental Study of Edge Plasma Structure in Various Discharges on Compact Helical System; Aug. 1996

NIFS-438 A. Komori, N. Ohyabu, S. Masuzaki, T. Morisaki, H. Suzuki, C. Takahashi, S. Sakakibara, K. Watanabe, T. Watanabe, T. Minami, S. Morita, K. Tanaka, S. Ohdachi, S. Kubo, N. Inoue, H. Yamada, K. Nishimura, S. Okamura, K. Matsuoka, O. Motojima, M. Fujiwara, A. Iiyoshi, C. C. Klepper, J.F. Lyon, A.C. England, D.E. Greenwood, D.K. Lee, D.R. Overbey, J.A. Rome, D.E. Schechter and C.T. Wilson,
Edge Plasma Control by a Local Island Divertor in the Compact Helical System; Sep. 1996 (IAEA-CN-64/C1-2)

NIFS-439 K. Ida, K. Kondo, K. Nagaski T. Hamada, H. Zushi, S. Hidekuma, F. Sano, T. Mizuuchi, H. Okada, S. Besshou, H. Funaba, Y. Kurimoto, K. Watanabe and T. Obiki,
Dynamics of Ion Temperature in Heliotron-E; Sep. 1996 (IAEA-CN-64/CP-5)

NIFS-440 S. Morita, H. Idei, H. Iguchi, S. Kubo, K. Matsuoka, T. Minami, S. Okamura, T.

Ozaki, K. Tanaka, K Toi, R. Akiyama, A. Ejiri, A. Fujisawa, M. Fujiwara, M. Goto, K. Ida, N. Inoue, A. Komori, R. Kumazawa, S. Masuzaki, T Morisaki, S. Muto, K. Narihara, K. Nishimura, I. Nomura, S. Ohdachi, M.. Osakabe, A. Sagara, Y Shirai, H. Suzuki, C. Takahashi, K. Tsumori, T. Watari, H. Yamada and I. Yamada,
A Study on Density Profile and Density Limit of NBI Plasmas in CHS; Sep. 1996 (IAEA-CN-64/CP-3)

NIFS-441 O. Kaneko, Y. Takeiri, K. Tsumori, Y. Oka, M. Osakabe, R. Akiyama, T. Kawamoto, E. Asano and T. Kuroda,
Development of Negative-Ion-Based Neutral Beam Injector for the Large Helical Device; Sep. 1996 (IAEA-CN-64/GP-9)

NIFS-442 K. Toi, K.N. Sato, Y. Hamada, S. Ohdachi, H. Sakakita, A. Nishizawa, A. Ejiri, K. Narihara, H. Kuramoto, Y. Kawasumi, S. Kubo, T. Seki, K. Kitachi, J. Xu, K. Ida, K. Kawahata, I. Nomura, K. Adachi, R. Akiyama, A. Fujisawa, J. Fujita, N. Hiraki, S. Hidekuma, S. Hirokura, H. Idei, T. Ido, H. Iguchi, K. Iwasaki, M. Isobe, O. Kaneko, Y. Kano, M. Kojima, J. Koog, R. Kumazawa, T. Kuroda, J. Li, R. Liang, T. Minami, S. Morita, K. Ohkubo, Y. Oka, S. Okajima, M. Osakabe, Y. Sakawa, M. Sasao, K. Sato, T. Shimpo, T. Shoji, H. Sugai, T. Watari, I. Yamada and K. Yamauti,
Studies of Perturbative Plasma Transport, Ice Pellet Ablation and Sawtooth Phenomena in the JIPP T-IIU Tokamak; Sep. 1996 (IAEA-CN-64/A6-5)

NIFS-443 Y. Todo, T. Sato and The Complexity Simulation Group,
Vlasov-MHD and Particle-MHD Simulations of the Toroidal Alfvén Eigenmode; Sep. 1996 (IAEA-CN-64/D2-3)

NIFS-444 A. Fujisawa, S. Kubo, H. Iguchi, H. Idei, T. Minami, H. Sanuki, K. Itoh, S. Okamura, K. Matsuoka, K. Tanaka, S. Lee, M. Kojima, T.P. Crowley, Y. Hamada, M. Iwase, H. Nagasaki, H. Suzuki, N. Inoue, R. Akiyama, M. Osakabe, S. Morita, C. Takahashi, S. Muto, A. Ejiri, K. Ida, S. Nishimura, K. Narihara, I. Yamada, K. Toi, S. Ohdachi, T. Ozaki, A. Komori, K. Nishimura, S. Hidekuma, K. Ohkubo, D.A. Rasmussen, J.B. Wilgen, M. Murakami, T. Watari and M. Fujiwara,
An Experimental Study of Plasma Confinement and Heating Efficiency through the Potential Profile Measurements with a Heavy Ion Beam Probe in the Compact Helical System; Sep. 1996 (IAEA-CN-64/C1-5)

NIFS-445 O. Motojima, N. Yanagi, S. Imagawa, K. Takahata, S. Yamada, A. Iwamoto, H. Chikaraishi, S. Kitagawa, R. Maekawa, S. Masuzaki, T. Mito, T. Morisaki, A. Nishimura, S. Sakakibara, S. Satoh, T. Satow, H. Tamura, S. Tanahashi, K. Watanabe, S. Yamaguchi, J. Yamamoto, M.Fujiwara and A. Iiyoshi,
Superconducting Magnet Design and Construction of LHD; Sep. 1996 (IAEA-CN-64/G2-4)

NIFS-446 S. Murakami, N. Nakajima, S. Okamura, M. Okamoto and U. Gasparino,
Orbit Effects of Energetic Particles on the Reachable β–Value and the Radial Electric Field in NBI and ECR Heated Heliotron Plasmas; Sep. 1996 (IAEA-CN-64/CP -6) Sep. 1996

NIFS-447 K. Yamazaki, A. Sagara, O. Motojima, M. Fujiwara, T. Amano, H. Chikaraishi, S. Imagawa, T. Muroga, N. Noda, N. Ohyabu, T. Satow, J.F. Wang, K.Y. Watanabe, J. Yamamoto , H. Yamanishi, A. Kohyama, H. Matsui, O. Mitarai, T. Noda, A.A. Shishkin, S. Tanaka and T. Terai
Design Assessment of Heliotron Reactor; Sep. 1996 (IAEA-CN-64/G1-5)

NIFS-448 M. Ozaki, T. Sato and the Complexity Simulation Group,
Interactions of Convecting Magnetic Loops and Arcades; Sep. 1996

NIFS-449 T. Aoki,
Interpolated Differential Operator (IDO) Scheme for Solving Partial Differential Equations; Sep. 1996

NIFS-450 D. Biskamp and T. Sato,
Partial Reconnection in the Sawtooth Collapse; Sep. 1996

NIFS-451 J. Li, X. Gong, L. Luo, F.X. Yin, N. Noda, B. Wan, W. Xu, X. Gao, F. Yin, J.G. Jiang, Z. Wu., J.Y. Zhao, M. Wu, S. Liu and Y. Han,
Effects of High Z Probe on Plasma Behavior in HT-6M Tokamak; Sep. 1996

NIFS-452 N. Nakajima, K. Ichiguchi, M. Okamoto and R.L. Dewar,
Ballooning Modes in Heliotrons/Torsatrons; Sep. 1996 (IAEA-CN-64/D3-6)

NIFS-453 A. Iiyoshi,
Overview of Helical Systems; Sep. 1996 (IAEA-CN-64/O1-7)

NIFS-454 S. Saito, Y. Nomura, K. Hirose and Y.H. Ichikawa,
Separatrix Reconnection and Periodic Orbit Annihilation in the Harper Map; Oct. 1996

NIFS-455 K. Ichiguchi, N. Nakajima and M. Okamoto,
Topics on MHD Equilibrium and Stability in Heliotron / Torsatron; Oct. 1996

NIFS-456 G. Kawahara, S. Kida, M. Tanaka and S. Yanase,
Wrap, Tilt and Stretch of Vorticity Lines around a Strong Straight Vortex Tube in a Simple Shear Flow; Oct. 1996

NIFS-457 K. Itoh, S.- I. Itoh, A. Fukuyama and M. Yagi,
Turbulent Transport and Structural Transition in Confined Plasmas; Oct. 1996

NIFS-458 A. Kageyama and T. Sato,
Generation Mechanism of a Dipole Field by a Magnetohydrodynamic Dynamo; Oct. 1996